inorganics

MDPI

Article

Carbon-$NiTiO_2$ Nanosorbent as Suitable Adsorbents for the Detoxification of Zn^{2+} Ions via Combined Metal–Oxide Interfaces

Azizah A. Algreiby *, Abrar S. Alnafisah, Muneera Alrasheedi, Tahani M. Alresheedi, Ajayb Alresheedi, Abuzar Albadri and Abueliz Modwi

Department of Chemistry, College of Science, Qassim University, Buraydah 51452, Saudi Arabia; mu.alrasheedi@qu.edu.sa (M.A.); tm.alrashidi@qu.edu.sa (T.M.A.); rshiedyas@qu.edu.sa (A.A.); aa.albadri@qu.edu.sa (A.A.); ab.khalid@qu.edu.sa (A.M.)

* Correspondence: grieby@qu.edu.sa

Abstract

Metal ions exemplify one of the most harmful and environmentally detrimental contaminants of water systems. This work describes the creation of an innovative chelated carbon-doped nickel and titanium oxide (C-$NiTiO_2$) hybrid as an adsorbent for the effective elimination of metal ions. The dominance of the TiO_2 anatase phase with a ≈ 61 nm crystallite size was verified by XRD and Raman investigation. Morphology investigations exposed polygonal nanoparticles consisting of Ti, C, Ni, and O. The nanostructure exhibited a surface area of 17 $m^2 \cdot g^{-1}$, a pore diameter of ≈1.5 nm, and a pore volume of 0.0315 $cm^3 \cdot g^{-1}$. The nanostructure was evaluated for the elimination of Zn (II) ions from an aqueous solution. The metal ion adsorption onto the hybrid nanomaterial was described and comprehended using adsorption kinetics and equilibrium models. The adsorption data matched well with the pseudo-second-order kinetics and Langmuir adsorption models, indicating a monolayer chemisorption mechanism and achieving a maximum Zn (II) ion elimination of 369 $mg \cdot g^{-1}$. Mechanistic investigation indicated film diffusion-controlled adsorption through inner-sphere complexation. The nanosorbent could be regenerated and reused for four rounds without appreciable activity loss, thus demonstrating its potential for water cleanup applications.

Keywords: C-$NiTiO_2$; Zn (II) ions adsorption; regeneration cycles; mechanism; water treatment

1. Introduction

The rapid progression of industrialization has resulted in a soaring demand for metals for use in numerous fields, such as batteries, explosives, coating materials, steel, oil refining, and pigments [1–3]. Apart from their usefulness as nutrients, metal ions are also accountable for increasing ecological pollution and thus warrant significant consideration owing to their potential threats to human well-being and environmental safety. Compared with organic toxic waste, metal ions, such as Hg (II), Zn (II), Ni (II), Pb (II), Cr (VI), Cu (II), and Fe (III), are difficult to degrade into harmless materials. They accumulate in organisms and are highly toxic or oncogenic [4]. Diverse conventional and modern procedures have been used to eliminate toxic metal ions from contaminated water. These approaches include electrochemical treatment [5], chemical precipitation, solvent extraction, oxidation/reduction, dialysis, ultra-filtration, ion exchange, reverse osmosis, adsorption, and membrane technologies [6]. Nonetheless, majority of these methods suffer from several downsides, for

Check for updates

Academic Editor: Chiara Dionigi

Received: 21 November 2025
Revised: 24 December 2025
Accepted: 28 December 2025
Published: 26 January 2026

Copyright: © 2026 by the authors. Licensee MDPI, Basel, Switzerland. This article is an open access article distributed under the terms and conditions of the Creative Commons Attribution (CC BY) license.

example, the generation of sludge mixed with contaminants as secondary pollution that requires further treatment, large chemical inputs, complexity, heavy infrastructure, and large capital investment [7]. On the other hand, adsorption processes are attractive methodologies for water treatment [8], mainly because adsorbents are inexpensive, do not require preliminary treatment before utilization, and are easy to regenerate. Therefore, adsorption is more desirable than other techniques because of its simplicity of design, convenience, and ease of operation [9]. Zinc is a trace element that is indispensable for human health and is an important metal for physiological tasks and the regulation of biochemical processes in living tissues. In spite of these benefits, excessive accumulation of zinc in the body can lead to abdominal cramps, epidermal irritations, spewing, queasiness, and anemia [10].

In recent times, there has been an upswing in the recognition of nanotechnology as a feasible and groundbreaking approach to tackling the difficulties linked to metal ion pollution in the environment. The use of TiO_2 for Zn (II) ion removal [11,12], polythiophene/TiO_2 [13], graphene-based TiO_2 [14], pure NiO [15], NiO–MgO silica-based nanoparticles [16], and NiO/chitosan nano-composites [17] has been explored. C-TiO_2 has been employed in photocatalytic activity such as (RhB) dye degradation [18], methylene blue degradation [19], nitrate reduction [20], and C-TiO_2/Ag for methyl orange degradation [21]. On the other hand, C-NiO has been employed for CR dye adsorption [22]; but, there is no research dealing with the application of C-$NiTiO_2$ in the adsorption of metal ions. The extensive use of TiO_2 can be attributed to its outstanding physicochemical, mechanical, and photocatalytic characteristics, besides its reactivity, thermal stability, low price, safety, biocompatibility, and capacity to be doped with other inorganic compounds. The main downside of nano-TiO_2 is its high agglomeration tendency; therefore, it is often associated with organic sources such as starch, gums, chitosan, or saccharides to diminish its spontaneous clustering and improve its functional properties. Carbon doping prevents the aggregation of nanoparticles, provides a high surface-to-volume ratio, and enhances surface area, pore volume, and porosity [23]. In addition, crystallite size decreases with C incorporation, which may be ascribed to C segregation at nanoparticle boundaries [24], as well as the generation of oxygen vacancies and lattice defects [25].

Zinc has many applications, such as electroplating, batteries, galvanized iron, and building materials; therefore, Zn (II) ions are present in effluents [26]. The recommended daily threshold for zinc intake are 15 mg, 25 mg, and 40 mg as set by the World Health Organization (WHO), European Food Safety Authority (EFSA), and Food and Drug Administration (FDA), respectively [27]. However, high-level zinc exposure due to the consumption of large quantities of zinc-containing foods or supplements in a short period of time has toxic effects. Signs of acute zinc toxicity include headache, nausea, vomiting, diarrhea, abdominal uneasiness, and, in occasional cases, metabolic imbalances and severe neurological symptoms [27]. The adsorption capacity of pristine TiO_2 for Zn (II) ions is barely 40.937 $mg \cdot g^{-1}$ [28], while sodium-doped TiO_2 achieves 93 $mg \cdot g^{-1}$ [29], indicating the low efficiency of TiO_2. Similarly, NiO shows low adsorption efficiency for Zn (II) ions, with adsorption capacities of 37.69 $mg \cdot g^{-1}$ for pure NiO [16], whereas CS can remove 61 $mg \cdot g^{-1}$ of Zn^{2+} from aqueous solutions [30].

In this setting, the current study tends to fabricate and characterize a composite constructed by integrating TiO_2 and NiO with a pyrolyzed carbon assembly. It is specifically designed to operate as an adsorbent to remove Zn (II) ions from aqueous environments. Batch experiments were conducted to assess the kinetic and thermodynamic features of the adsorption process. Furthermore, the recyclability and reusability of the porous C-$NiTiO_2$ adsorbent was explored, and a potential mechanism for the adsorption of metal ions was proposed.

2. Results and Discussion

2.1. Nanomaterials Characterizations

The phase configuration and peak assembly of C-$NiTiO_2$ are displayed in Figure 1a using X-ray diffraction (XRD) patterns. The facets of C-$NiTiO_2$ revealed quite sharp high intensities peaks demonstrating high crystallinity. The outcomes publicized that the as-synthesized C-$NiTiO_2$ was primarily composed of the anatase TiO_2 phase, aligning well polycrystalline tetragonal TiO_2 (JCPDS# 21−1272) [31]. This is evidenced by diffraction peaks at 2θ ≈ 25.38°, 37.0, 37.90°, 48.06°, 48.06, 53.92°, 55.16°, 62.79°, 68.79°, and 70.38°, which can be assigned to (101), (103), (004), (112), (200), (105), (211), (204), (116), and (220) crystal reflections [32]. Nonetheless, no diffraction signal corresponding to C or Ni phases were perceived in the XRD pattern of C-$NiTiO_2$. This may be ascribed to the low amount of these elements, which bring about a reduced diffraction intensity of C (below the recognition limit of the XRD machine), or to the interstitial doping of Ni^{2+} into Ti^{4+} due to the smaller ionic radius of Ni^{2+} (0.605 Å) relative to that of Ti^{4+} (0.690 Å). A related result was likewise reported [33]. The microstructural constants, including the size of crystallites (D), dislocation density (δ), inter-lattice distance (d), lattice constants (a, b, c), crystal volume (V), and microstrain (ε) for TiO_2 phase, were computed using the following expressions, and the corresponding values are listed in Table 1.

$$D = \frac{0.9\lambda}{\beta cos\theta} \quad (1)$$

$$\delta = \frac{1}{D^2} \quad (2)$$

$$d = \frac{\lambda}{2sin\theta} \quad (3)$$

$$\frac{1}{d^2} = \frac{h^2 + k^2}{a^2} + \frac{l^2}{c^2} \quad (4)$$

$$V = a \cdot b \cdot c \quad (5)$$

$$\varepsilon = \frac{\beta}{4tan\theta} \quad (6)$$

Table 1. XRD structural variables for the C-$NiTiO_2$ nanostructure.

Parameter	D (nm)	δ (nm^{-2})	d (Å)	Lattice Constants (Å)		V ($Å^3$)	ε
Value	60.85	0.0003	3.5011	a = b = 3.7833	c = 9.4881	135.81	0.0026

The terms λ, β, and θ denote the Cu K-α radiation source (0.15406 nm), the internal breadth of the Bragg's profiles, and the Bragg angle. The D value of 60.85 infers the development of a material within the nanoscale range. The lattice parameters were relatively less than the standard a = b = 3.782 and c = 9.5139 Å, which may be related to the incorporation of the smaller Ni (II) ions and C (r = 0.038 nm) [34]. The integration of aliovalent Ni (II) impurity ions into the TiO_2 host lattice as substitutional ions or interstitial dopants can either create an n-type free carrier or generate Ni vacancies (V_{Ni}) to guarantee charge balance. As smaller-radius dopant substitutes at Ti host locations, the lattice d-spacing is anticipated to decrease, and diffraction peaks shift to higher values [35], inducing a distortion of the lattice, which would be evident by a shrinkage in the lattice parameters [36].

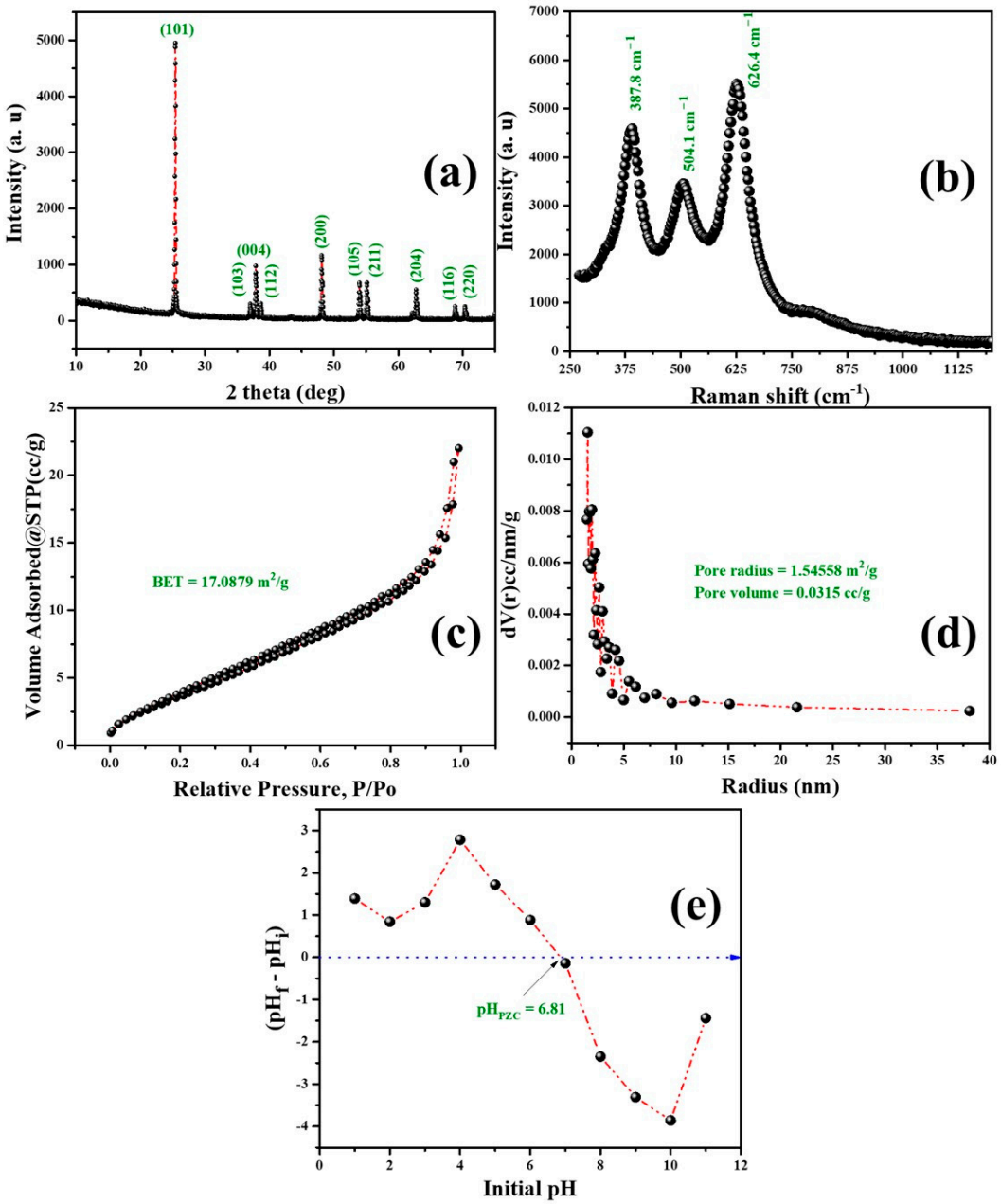


Figure 1. The XRD patterns (**a**), Raman spectrum (**b**), N_2-adsorption isotherm (**c**), pore size distribution (**d**), and pHpzc (**e**) for C-$NiTiO_2$.

Anatase TiO_2 is characterized to exhibit Raman activity peaks B_{1g} (387.8 cm^{-1}), overlaid A_{1g}-B_{1g} peaks (504.1 cm^{-1}), and the overtone of E_g (626.4 cm^{-1}), which were witnessed in the active vibrational mode shown in Figure 1b. Thus, Raman analysis also confirms the presence of the pure anatase phase of TiO_2 [37]. The N_2 adsorption−desorption isotherm presented in Figure 1c shows that the C-$NiTiO_2$ samples show a distinctive type IV isotherm with an H3 hysteresis loop in the P/P_0 range between 0.4 and 0.9, signifying the existence of well-developed mesopores in the sample. The corresponding pore size distribution curve is displayed in Figure 1d. Barrett−Joyner−Halenda analysis divulged that C-$NiTiO_2$ had a surface area of approximately 17 ± 0.56 $m^2 \cdot g^{-1}$, with a pore diameter and pore volume of ≈1.5 nm and 0.0315 $cm^3 \cdot g^{-1}$, respectively. The point of zero charge (pHpzc) refers to the pH at which the positive and negative charges on the surface of a solid are equal, resulting in a net charge of zero. pHpzc is a crucial property that significantly influences

the adsorption behavior of the adsorbent. Figure 1e shows the pHpzc for the C-$NiTiO_2$ sorbent as 6.81 ± 0.28.

SEM analysis was carried out to inspect the morphology of C-$NiTiO_2$. The obtained images, as shown in Figure 2a, reveal aggregated spherical structure nanoparticles with an average size of 250 nm. For elemental analysis, SEM in conjunction with energy-dispersive X-ray spectroscopy (EDS) was used to detect and quantify the main elements constituting C-$NiTiO_2$ (Figure 2b). From the EDS data, elemental Ni is determined at around 8 eV and titanium is at 4.5 eV, in addition to elemental C and O. The EDS spectrum indicates the successful development of C-$NiTiO_2$ NPs. Elemental mapping of the C-$NiTiO_2$ nanostructure was performed using low-magnification TEM portrayal (Figure 2c), with the corresponding elemental distribution depicted in Figure 2d. The exposed images in Figure 2d demonstrated that C, Ni, Ti, and O elements coexisted and were uniformly spread across the C-$NiTiO_2$ surface, attesting to the composition and purity of the sample, which agrees with the EDS results.

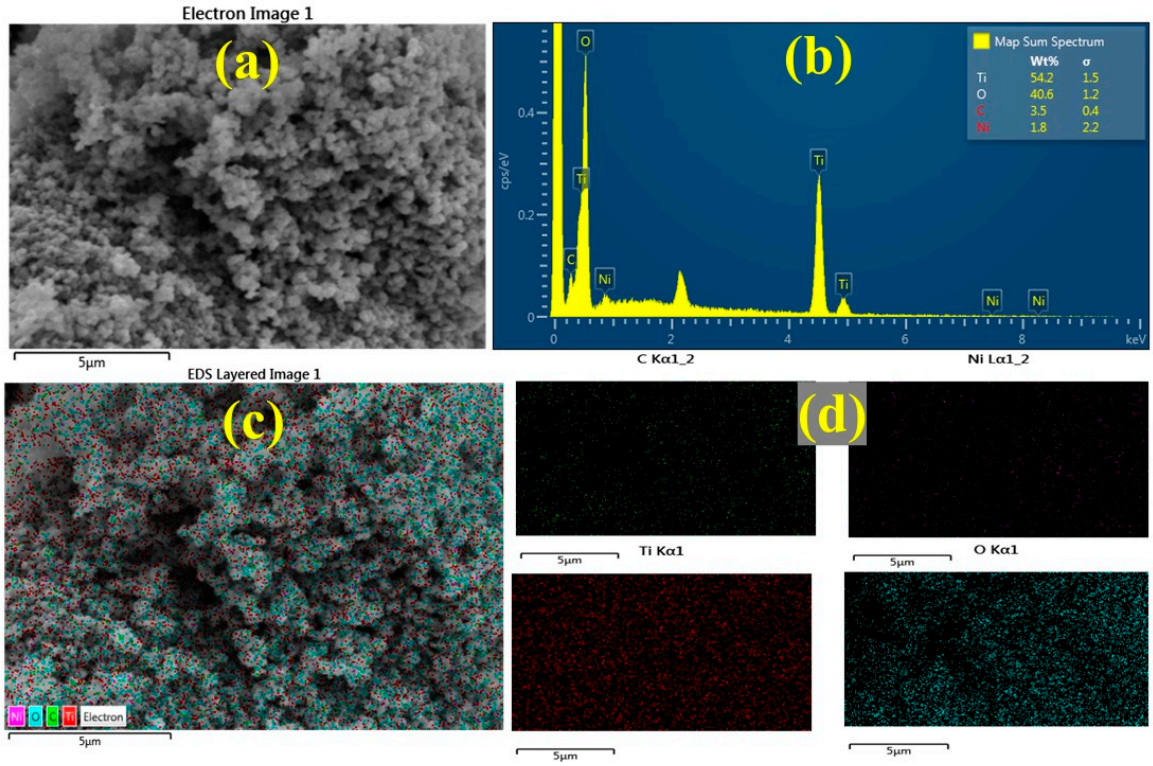


Figure 2. The SEM (**a**), EDC (**b**), and elemental color mapping (**c**,**d**) of C-$NiTiO_2$.

The morphology of C-$NiTiO_2$ was further envisaged by TEM images (Figure 3). The sample mainly consisted of marginally uniform polygonal structures, most likely composed of transparent TiO_2 nanoparticles with an average size of ≈200 nm (Figure 3a). Darker structures were also observed in Figure 3b, suggesting overlapping of the TiO_2 particles. In addition, tiny cluster particles were seen, which may indicate the presence of carbon. The SAED pattern (Figure 3c) displays diffraction rings that may be indexed according to 5.7/nm (101), 8.421/nm (004), and 13.561 (204) planes of TiO_2. The lattice distance of TiO_2 (Figure 3d) was found to be 0.4 nm, which is in good accord with the XRD d-spacing of 0.035 nm (Figure 1a) at the (101) reflection.

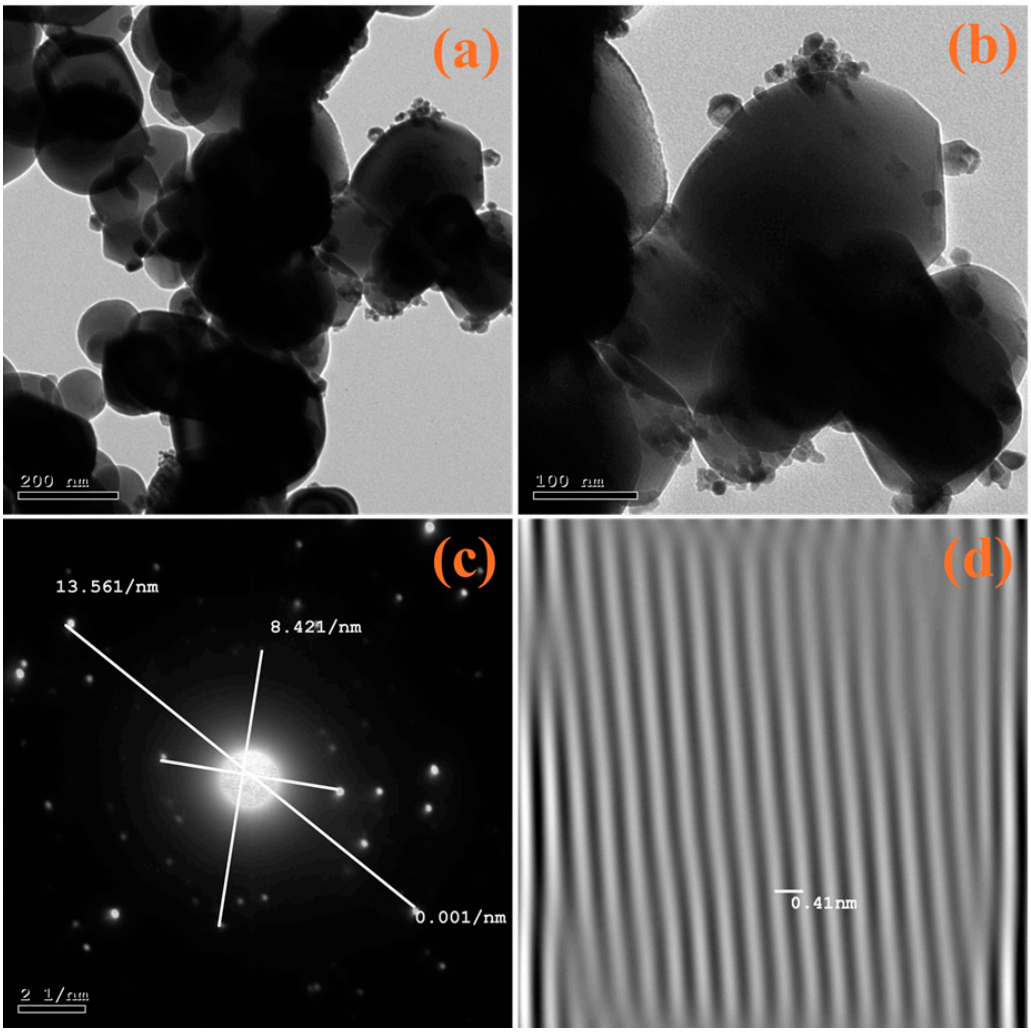


Figure 3. TEM patterns with different magnifications (**a**,**b**), SAED pattern, and lattice d-spacing of C-$NiTiO_2$ (**c**,**d**).

2.2. Zn (II) Ion Adsorption

The adsorption of Zn (II) ions was explored by changing the C-$NiTiO_2$ dosage from 2 to 12 mg L^{-1} under room temperature conditions at pH 3.5, and the responses are shown in Figure 4a. The percentage removal of Zn (II) ions increased with augmented adsorbent loading, which was ascribed to the larger surface area and greater availability of active functional groups, thereby boosting the accessibility of active binding spots in the C-$NiTiO_2$ nanostructure. Complete removal of metal ion adsorbates was achieved using a 12 mg L^{-1} dose. The designated methodology assessed the behavior of the adsorption process in line with disparities in the initial concentration of Zn (II) ions in solution. Thus, Figure 4b depicts that removal percentages and the adsorbed quantity q_t ($mg \cdot g^{-1}$) were inherently associated with the initial concentration of Zn (II) ions in the solution. As the metal ion concentration increased, the number of adsorptive species and the demand for active adsorption sites also increased. At high concentrations, the excess number of adsorptive molecules in solution restricted the number of sites accessible for adsorption, resulting in lower removal since the surface saturated readily [38]. Nevertheless, at lower concentrations, the number of possible adsorption sites was adequately large relative to the number of adsorptive molecules, so the surface was not easily saturated. It was observed that the q_t values increased sharply at lower initial Zn (II) ion concentrations owing to the numerous vacant sites, whereas the hike in adsorption of metal ions slowed as the concentration rose. The highest uptake quantity was attained at >300 $mg \cdot g^{-1}$ using an initial concentration of

200 mg L^{-1} [39]. The pH of the medium has a profound impact on the elimination of metal cations, as it influences speciation, the extent of metal ion precipitation in solution, and the chemical state of adsorbent binding sites, which eventually affects their tendency for target metal ions. The impact of solution pH on the adsorption efficiency of C-$NiTiO_2$ was probed over a pH range from 1 to 9 (Figure 4c). The results evidently demonstrated the strong pH dependency of the C-$NiTiO_2$ interaction with Zn (II) ions. The data showed that the maximum Zn (II) ion uptake occurred at pH = 3.5, decreased at pH = 5, and finally dropped to a minimum at pH = 7. In water, there are four types of zinc species: Zn (II) ions, $ZnOH^+$, Zn(O), and Zn $(OH)_2$. Since Zn $(OH)_2$ is highly soluble in the pH range of 1.0–5.0, Zn^{2+} is the key ion in solution. In addition, Zn (II) ions exist as hydrated species such as $Zn(H_2O)_6^{2+}$, $Zn(OH)(H_2O)_3^+$, and $Zn(OH)_2(H_2O)_2$, with an average coordination number of about 4.5 O atoms surrounding a core Zn atom at lower pH [40]. Obviously, under an acidic environment, the surface of TiO_2 was satisfactorily protonated and positively charged, which was supposed to be in strong electrostatic repulsion with Zn^{2+} cations and depress Zn (II) ion sorption. This anomaly of positive ion uptake at low pH may be justified by the formation of hydrated zinc species that bind to the adsorbent via an inner-sphere complexation mechanism. Similar behavior has been reported for Sr (II), which was attributed to inner-sphere complexes at high pH and inner-sphere complexes at low and intermediate pH [41]. The increased Zn (II) ion adsorption at pH = 8 could be explained by the precipitation of Zn (II) as hydroxide.

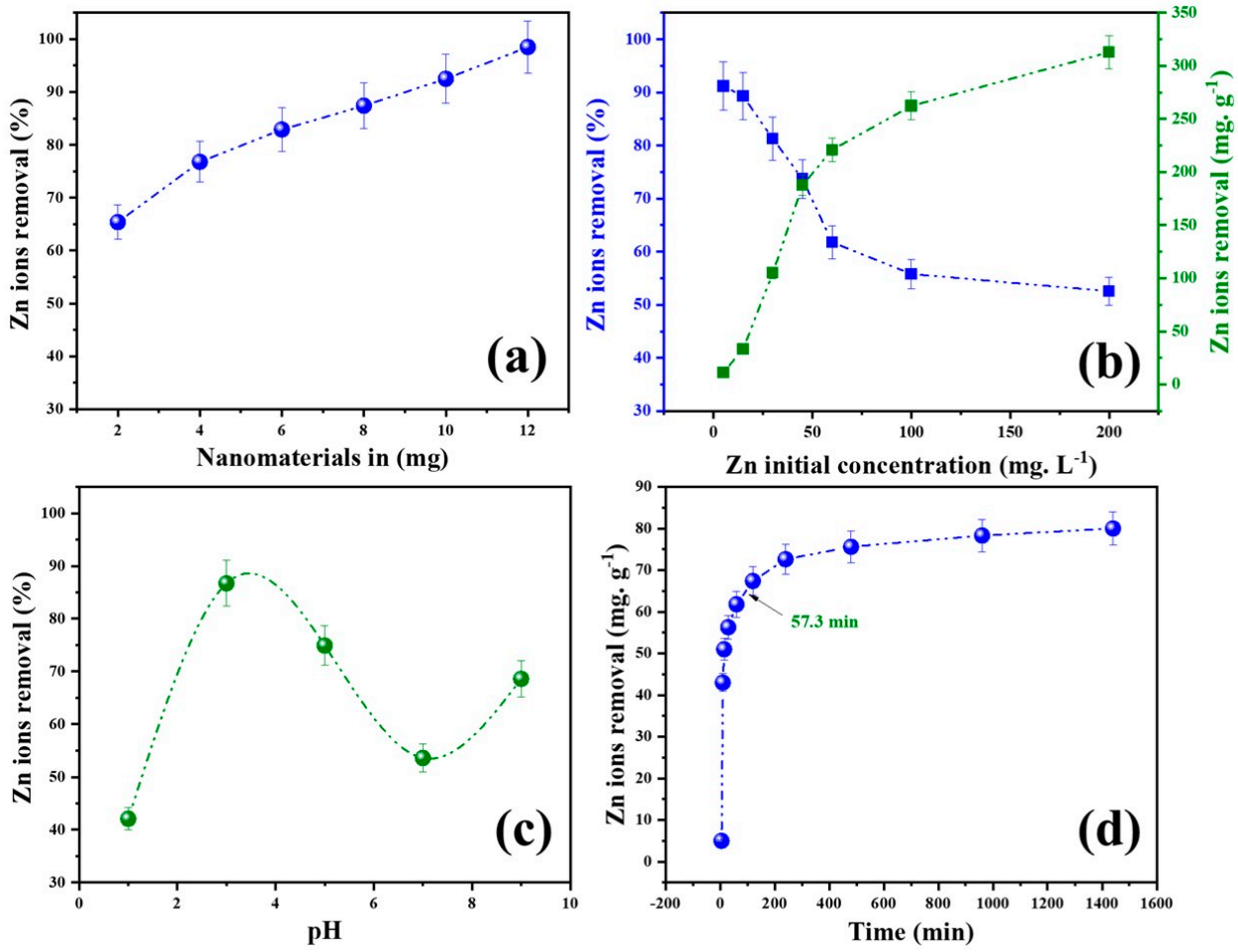


Figure 4. Effects of adsorbent dose (**a**), initial concentration (**b**), solution pH (**c**), and contact time (**d**) on Zn (II) ion adsorption by C-$NiTiO_2$ (Conditions: Initial concentration = 45 mg·L^{-1}, Zn (II) volume = 25 mL, Nanosorbent mass = 10 mg, Contact time = 1440 min).

The adsorption efficiency of C-$NiTiO_2$ nanoparticles towards Zn (II) ions was explored by batch equilibrium procedures for contact durations varying between 0 and 1400 min, and the result is displayed in Figure 4d. The high rate of Zn (II) ion uptake that occurs spontaneously at diminutive contact times was concomitant with the large number of active sites accessible on the surface of the nanoparticles. Nonetheless, as contact time elapsed, metal ions increasingly adhered to these sites [42]. The rate of metal ion sorption then became constant after attaining equilibrium at 57 min, as demonstrated by the plateau on the curve in Figure 4d, achieving a maximum adsorption capacity of q_e = 70 mg·g^{-1} and ≈80% removal.

The adsorption kinetics provide insight into the time-based equilibrium of adsorption, the mechanism dominating the process, and the rate at which metal ions cling to the adsorbent. For C-$NiTiO_2$, the adsorption behavior of Zn (II) ions was surveyed using pseudo-first-order kinetics (PFO), pseudo-second-order kinetics (PSO), Elovich, and intraparticle diffusion models [3], as shown in Table 2 and Figure 5a–d. The PSO model conveys a physisorption method, and diffusion is deliberated as the rate-controlling step. For the PSO model, the rate-limiting step is typically a chemisorption process, which includes the sharing or interchange of electrons between the intermingling adsorbate and adsorbent surface, while the Elovich formula defines the kinetics of chemical adsorption schemes. The model is quite appropriate for heterogeneous surfaces [43]. By comparing the regression coefficients (R^2) of the three adsorption kinetic models, the PSO kinetic model exhibited the highest correction coefficients (R^2 = 0.9992), suggesting that the PSO kinetic model best fits the adsorption kinetics of Zn (II) ions on C-$NiTiO_2$ NPs, as shown in Figure 5b and Table 3. In addition, the computed equilibrium capacity $q_{e\cdot cal}$ (81.10 mg·g^{-1}) estimated from the PSO kinetic model was almost equal to the experimental equilibrium capacity $q_{e\cdot exp}$ (80.0 mg·g^{-1}) compared to the other two models. It is worth noting that the lowest *RSS* value (0.5358) for the PSO model reaffirms its suitability for describing the kinetic data. These annotations indicate that the retention of Zn (II) ions involves chemical interactions, implying a chemisorption process [30]. Deviating from the origin, the fitted internal particle diffusion plot exhibited a nonlinear relationship between q_t and $t^{1/2}$. This remark proposes that internal diffusion process did not singularly control the rate-determining stage, and that Zn (II) ion adsorption rate could be affected by external diffusion [44]. The adsorption process was demarcated into two steps. The primary phase involves surface layer adsorption, wherein Zn (II) ions dwell active adsorption sites on the outer surface of C-$NiTiO_2$. The succeeding stage corresponds to intraparticle diffusion, where Zn (II) ions surmount the barrier enforced by the outer liquid film and infuse toward the internal surface of C-$NiTiO_2$. This stage characterizes the quasi-equilibrium adsorption stage. The diffusion rate constants in the two stages follow the sequence $k_{dif1} > k_{dif1}$, which is also evident from the model drafted in Figure 5d. The earlier step of the experiment showed a speedy gush in adsorption, establishing a rapid adsorption activity delineated by the steeper slope at the very short 10 min time duration. Then, the adsorption rate slowly leveled off until reaching 40 min. This period resembled a slow Zn (II) ion uptake that proceeded towards dynamic equilibrium, as evidenced by a zero-approaching slope. Thus, the kinetic investigations manifested that Zn (II) ion adsorption on C-$NiTiO_2$ is a chemisorption process administered by both internal and external diffusion [45]. To predict whether film diffusion or intraparticle diffusion is the rate-limiting step, the Boyd plot was tested. As per this model, IPD is considered the rate-determining step if the plot of B_t (computed via Equation (7) or Equation (8)) versus time gives a straight line transversing the origin. If the Boyd plot is nonlinear, or linear but does not pass through the (0, 0) point, it can be concluded that the regulating step is attributed to film diffusion or a chemical reaction [46].

$$B_t = 2\pi - \frac{\pi^2 F}{3} - 2\pi\left(1 - \frac{\pi F}{2}\right)^{1/2} \quad (7)$$

$$B_t = 0.4977 - ln(1 - F) \quad (8)$$

Table 2. Adsorption kinetic model equations [47].

Kinetics Models	Linear Equations	Plot	Calculated Coefficients
pseudo-first-order	$ln(q_e = q_t) = ln\frac{lq_e - k_1 t}{2.303}$	$ln(q_e - q_t)$ vs. t	$k_1 = -slopex2.303$ $q_e = e^{-intercepy}$
pseudo-second-order	$\frac{1}{q_t} = \frac{1}{k_2 x q_e^2} + \frac{t}{q_e}$	$\frac{t}{q_t}$ vs. t	$k_2 = \frac{slope^2}{intercept}$ $q_e = slope^{-1}$
Elovich	$q_t = \frac{1}{\beta} ln\alpha\beta + \frac{1}{\beta} lnt$	q_t vs. t	
intraparticle diffusion	$q_t = k_{dif} t^{0.5} + C$	q_t vs. $t^{0.5}$	$k_{dif} = slope$ C = intercept
Boyd model	$\beta_t = -0.4977 - \ln(1 - \frac{q_t}{q_e})$	β_t vs. t	$B = slope$

k_1 (min^{-1}) and k_2 ($g{\cdot}mg^{-1}{\cdot}min^{-1}$) represent the rate constants for the pseudo-first-order and pseudo-second-order reactions, respectively; q_t indicates the adsorption quantity of metal ions at time t ($mg{\cdot}g^{-1}$), and q_e signifies the equilibrium adsorption quantity ($mg{\cdot}g^{-1}$), while t denotes the contact time (min). α is the initial adsorption rate (mg/g·min), and β is the desorption constant.

Table 3. The adsorption kinetic constants for Zn ion adsorption on C-$NiTiO_2$ nanostructure.

PFO Model		PSO Model		Elovich Model		IPD Model			
k_1	0.0032	k_2	0.0005	β	0.9753	Stage 1		Stage 2	
q_e	28.90	$q_{e(exp)}$	80.00			K_{dif1}	5.9277	K_{dif2}	0.2524
		$q_{e(calc)}$	81.10	$\alpha \times 10^{-3}$	126.7	C1	33.399	C2	96.419
R^2	0.9108	R^2	0.9992	R^2	0.8405	R^2	0.9797	R^2	0.9810
RSS	1.814	*RSS*	0.5358	*RSS*	10.246	RSS	78.715	RSS	0.7309

As observed from the graph in Figure 5e, the plot was nonlinear, denoting that the film diffusion step was dominantly controlling the diffusion of Zn (II) ions into the C-$NiTiO_2$ adsorbent.

The adsorbent/adsorbate interactions at adsorption equilibrium can be predicted using adsorption isotherm models (Figure 6a–d linear models and Figure 6e nonlinear fitting for all models used. Within the dominion of isothermal sorption, four commonly adopted models, like Langmuir, Freundlich, D–R, and Temkin, were implemented to fit the isothermal sorption data (Table 4 and Figure 6) [3]. On the surface of the adsorbent, the Langmuir adsorption isotherm assumes a perfect monolayer and homogeneous dispersal of equivalent sorption sites with equal energy, whereas the Freundlich isotherm model represents an empirical style of multilayer adsorption with non-ideal and non-uniform distribution of sorption sites with different affinities. From the tabulated results in Table 5, Zn (II) ion adsorption was well presented by the Langmuir isotherm model, where the correlation factor (R^2 = 0.9983) was the highest compared to other models. In addition, the smallest chi-square value (χ^2 = 0.00011) affirmed the appropriateness of the Langmuir model. The maximum adsorption capacity of Zn (II) ions onto C-$NiTiO_2$, as determined by the Langmuir model, was 369 $mg{\cdot}g^{-1}$. In addition, the R_L ($R_L = 1/(1 + K_L C_0)$ of the Langmuir model for the metal ions lies within the 0–1 range, denoting advantageous adsorption of Zn (II) ions onto the C-$NiTiO_2$ adsorbent [42]. The adsorption intensity n (n = 1.524) obtained from the Freundlich model was in the 1–10 limit, signifying favorable adsorption activity [43].

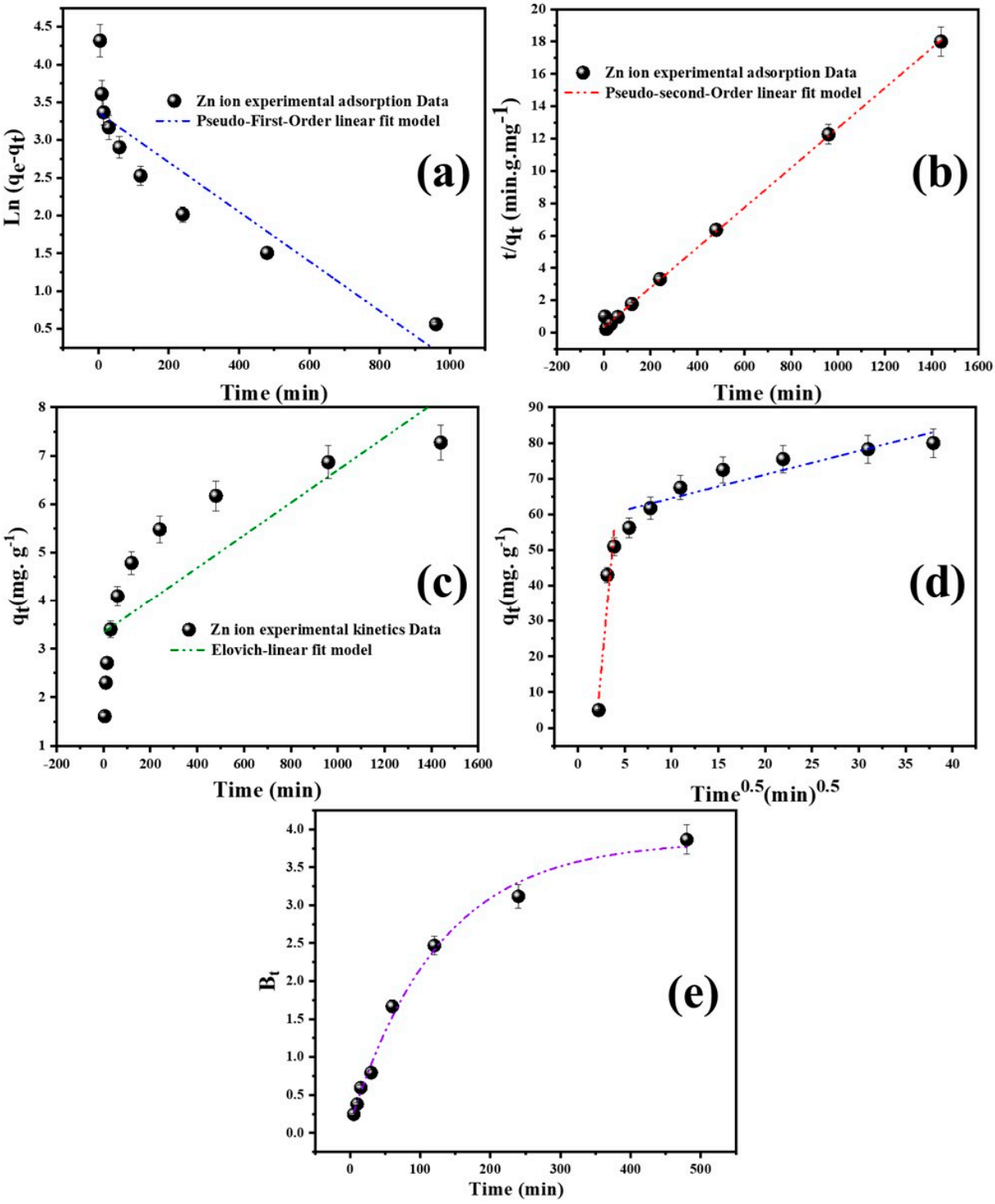


Figure 5. The PFO (**a**), PSO (**b**), Elovich (**c**), IPD (**d**), and Boyd (**e**) kinetic model for Zn (II) ions on C-$NiTiO_2$ (Conditions: Initial concentration = 45 mg·L^{-1}, Zn (II) volume = 150 mL, Nanosorbent mass = 60 mg, Contact time = 1440 min).

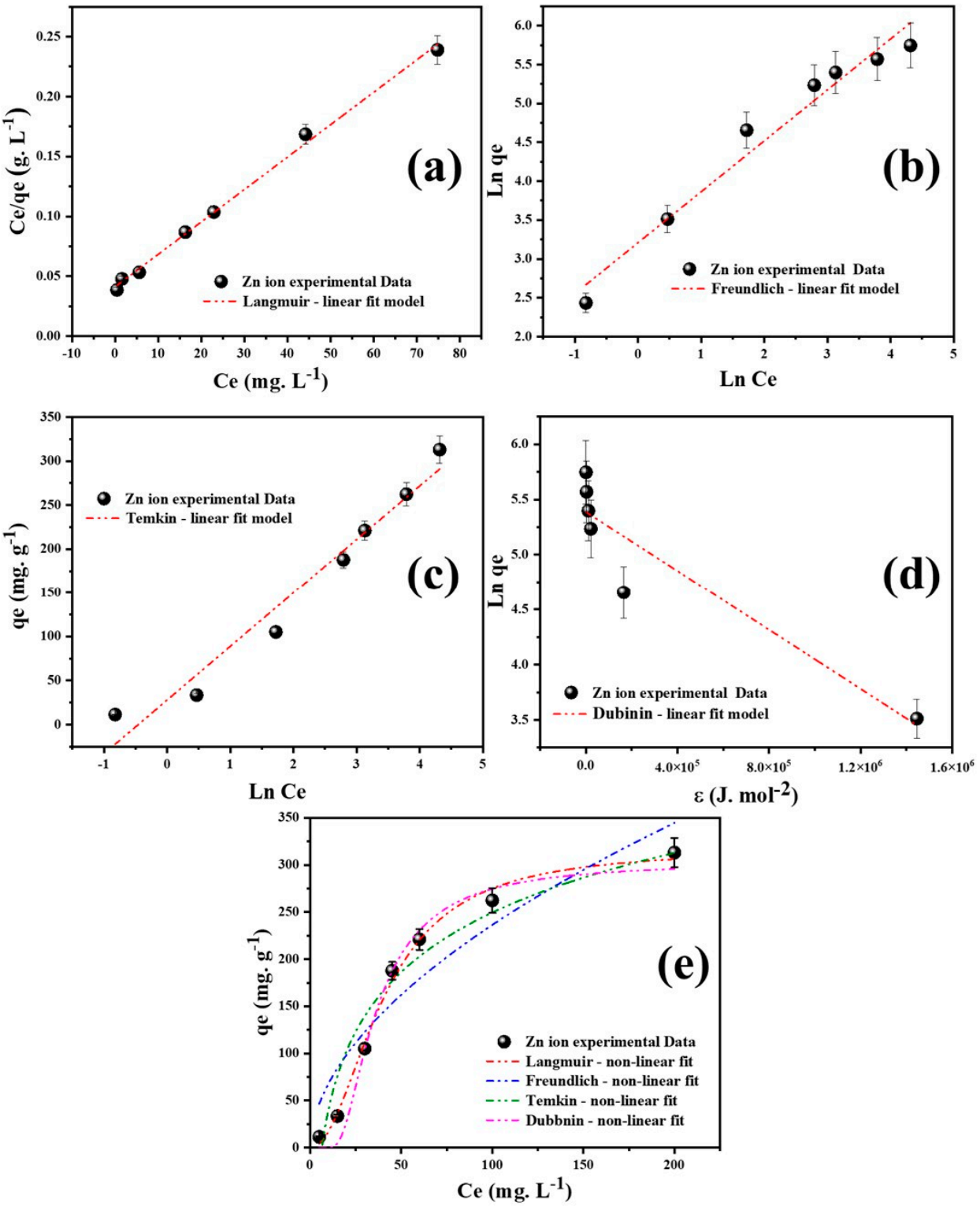


Figure 6. The Langmuir (**a**), Freundlich (**b**), Temkin (**c**), D–R (**d**) Linear isotherm model and Non-linear models (**e**) for Zn (II) ions on C-$NiTiO_2$ (Conditions: Initial concentration = 5, 15, 30, 45, 60, 100 and 200 mg·L^{-1}, Zn (II) volume = 25 mL, Nanosorbent mass = 10 mg, Contact time = 1440 min).

Table 6 provides a comparison of the adsorption performance of C-$NiTiO_2$ towards Zn (II) ion uptake alongside other adsorbents documented in the literature. The data show similarities in experimental parameters, as most adsorption process were monolayer and chemical in nature. Nevertheless, C-$NiTiO_2$ showed a higher quantity of eliminated metal ions despite the relatively lower pH and lower adsorbent dose. The lower adsor-

bate/adsorbent ratio indicates less secondary sludge waste. Furthermore, high recyclability and reusability add economic value.

Table 4. Adsorption isotherm model equations [48].

Models	Linear Equations	Plot	Calculated Coefficients
Langmuir	$\frac{C_e}{q_e} - \frac{1}{q_m K_L} + \frac{C_e}{q_e}$	$\frac{C_e}{q_e}$ vs. C_e	$K_L = \frac{slope}{intercept}$ $q_m = slope^{-1}$
Freundlich	$logq_e = logK_F + log\frac{C_e}{n}$	$logq_e$ vs. $logC_e$	$K_F = 10^{intercept}$ $n = slope^{-1}$
Temkin	$q_e = \frac{RT}{b_T} + \beta lnC_e$	lnC_e vs. q_e	$B = \frac{RT}{b_T}$ = intercept
Dubinin–Radushkevich	$lnq_e = lnq_m - (\beta\varepsilon^2)$	ε vs. lnC_e	$q_m = e^{-intercept}$ $\beta = e^{-slope}$

The adsorbate concentration in solution ($mg{\cdot}L^{-1}$) at equilibrium and the amount adsorbed ($mg{\cdot}g^{-1}$) are indicated as q_e and C_e, respectively. K_L is the Langmuir constant ($L{\cdot}mg^{-1}$), and q_m indicates the maximum adsorption capacity of the monolayer formed on the adsorbent. K_F and n stand for the Freundlich isotherm constants, indicating the adsorption capacity ($mg{\cdot}g^{-1}$) and adsorption intensity (dimensionless), respectively. T = absolute temperature (K), R = gas constant, *and* $\varepsilon = RTln\left[1 + \frac{1}{C_e}\right]$.

Table 5. Isotherm constant models for Zn (II) ion adsorption onto C-$NiTiO_2$ nanostructure.

Langmuir					Freundlich			
q_m ($mg{\cdot}g^{-1}$)	K_L ($mg{\cdot}g^{-1}$)	R_L ($L{\cdot}mg^{-1}$)	R^2	χ^2	n	K ($L{\cdot}mg^{-1}$)	R^2	χ^2
369	0.0657	0.3366	0.9983	0.00011	1.524	24.70	0.9827	0.3136
Dubinin–Radushkevich					**Temkin**			
q_m ($mg{\cdot}g^{-1}$)	β ($mol{\cdot}KJ^{-1})^2$	E (KJ/mol)	R^2	χ^2	B ($J{\cdot}mol^{-1}$)	b_T ($L{\cdot}mg^{-1}$)	R^2	χ^2
218.3	1.338	1.63	0.9328	0.4449	40.649	1.562	0.9807	0.3041

Table 6. Comparative adsorption capacity and experimental conditions for the removal of Zn (II) ions.

Adsorbent	$[Zn^{2+}]$ ($mg{\cdot}L^{-1}$)	Dose (mg/100 mL)	Kinetics	pH	q_{max} ($mg{\cdot}g^{-1}$)	Ref.
PSP	100	25	PSO	6.5	130.54	[49]
Zr-MOF-808	20	20	PSO	4.6	287.06	[3]
Agave bagasse	100	400	PSO	5.5	24.660	[50]
EDTA-silica	60	60	PSO	5.5	27.160	[51]
Sugarcane bagasse	50	100	-	6.0	40.000	[52]
PATDC	100	100	PSO	6.0	226.70	[53]
Chitosan–PVA	10	5000	PSO	5	5.0000	[54]
C-$NiTiO_2$	50	15	PSO	3.5	369.00	This work

2.3. Mechanism of Zn (II) Ion Adsorption

To elucidate the adsorption of Zn (II) ions by the C-$NiTiO_2$ nanocomposite, FTIR spectra of the adsorbent were recorded before and after the adsorption process. The adsorption process is postulated to take place through the following mechanisms:

1. Ion exchange: when adsorbents have functional groups containing protons on oxygen atoms, such as hydroxyl, metal ions can easily exchange with H^+ on oxygen sites.

$$–OH + M^{n+} \rightarrow –O...M + nH^+$$

$$–2OH + M^{n+} \rightarrow –O...M...O^- + nH^+$$

2. Surface complexation: This is another significant mechanism for removing metal ions, whether it is inner- or outer-sphere complexation. In this mechanism, complex formation takes place through the interaction between donor and acceptor electron pairs. Regardless of whether they constitute simple substances or compounds, acceptors usually include metal ions, while donors are atoms or ions able to provide electron pairs. Furthermore, through inner-sphere complexation, Zn (II) ions are bonded to free hydroxyl (O–H) functional groups, which was indicated by the disappearance of 3496 cm^{-1} after the adsorption of Zn (II) ions (Figure 7). The metal ions were mostly adsorbed through surface complexation between the lone pair electrons of oxygen atoms in –OH groups and the vacant electron orbitals of Zn (II) ion, according to their mechanistic analysis [55].

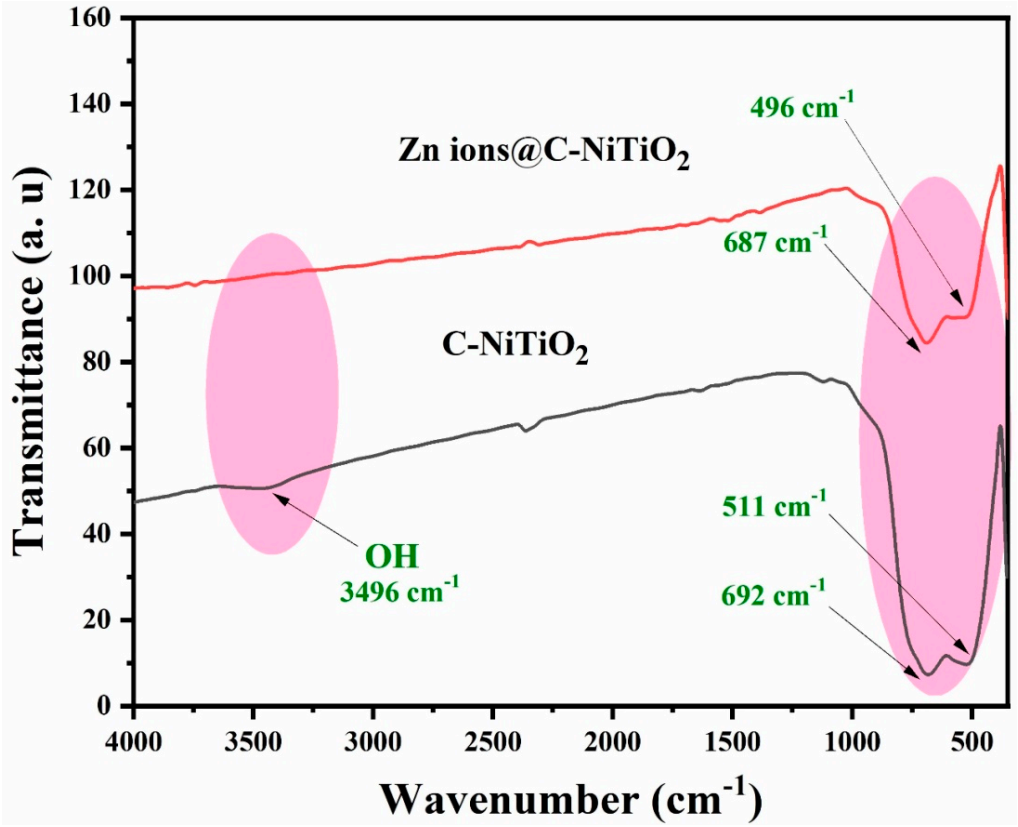
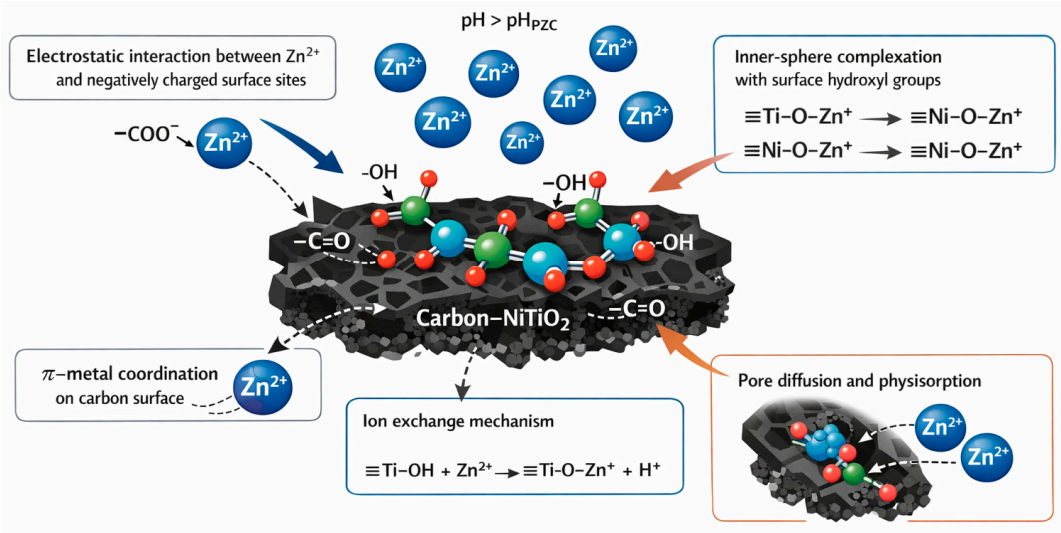


Figure 7. FTIR spectra of the C-$NiTiO_2$ composites before and after the adsorption of Zn (II) ions.

3. Electrostatic attraction: Charged Zn (II) ions can adsorb onto differently charged adsorbents, as metals ions have a dynamic affinity for surface hydroxyl (OH) groups.
4. As evidenced in the characterization section, C-$NiTiO_2$ exhibits a typical porous structure with a pore diameter of ≈1.5 nm and a pore volume of 0.0315 $cm^3 \cdot g^{-1}$, which offers plenty of active sites via a film diffusion mechanism, as derived from Boyd's kinetic model.

The reduction in M–O bonds and their shift to lower wavenumbers, from 692 to 678 cm^{-1} and from 511 to 496 cm^{-1}, support the adsorption of Zn (II) ions onto the composite surface. Based on the FTIR wavenumber equation $\tilde{\nu}(cm^{-1}) \alpha \sqrt{\frac{k}{\mu}}$, the replacement of lighter Ti (47.87) or Ni (58.69) atoms by heavier Zn (65.38) leads to a shift toward lower wavenumbers [56]. Scheme 1 portrays the presumed adsorption mechanism of the adsorption of Zn (II) ions onto the C-$NiTiO_2$ composite.



Scheme 1. Proposed mechanism of Zn (II) ion adsorption by the C-$NiTiO_2$ composite.

After Zn (II) ion adsorption onto the C-$NiTiO_2$ surface, the morphology and elemental composition of the constructed material were studied again by EDS to confirm adsorption ability. In Figure 8a,b, the elemental composition data and EDX mapping showed the appearance of a Zn peak, indicating effective adsorption of Zn (II) ions onto the surface of C-$NiTiO_2$ while retaining the aggregated spherical nanostructures. Elemental mapping of adsorbed Zn (II) ions on the surface of nanostructures exhibits a uniform distribution of Zn ions across the C-$NiTiO_2$ surface (Figure 8c–f). These results give further evidence that the C-$NiTiO_2$ nanosorbent was successfully developed for zinc ion removal.

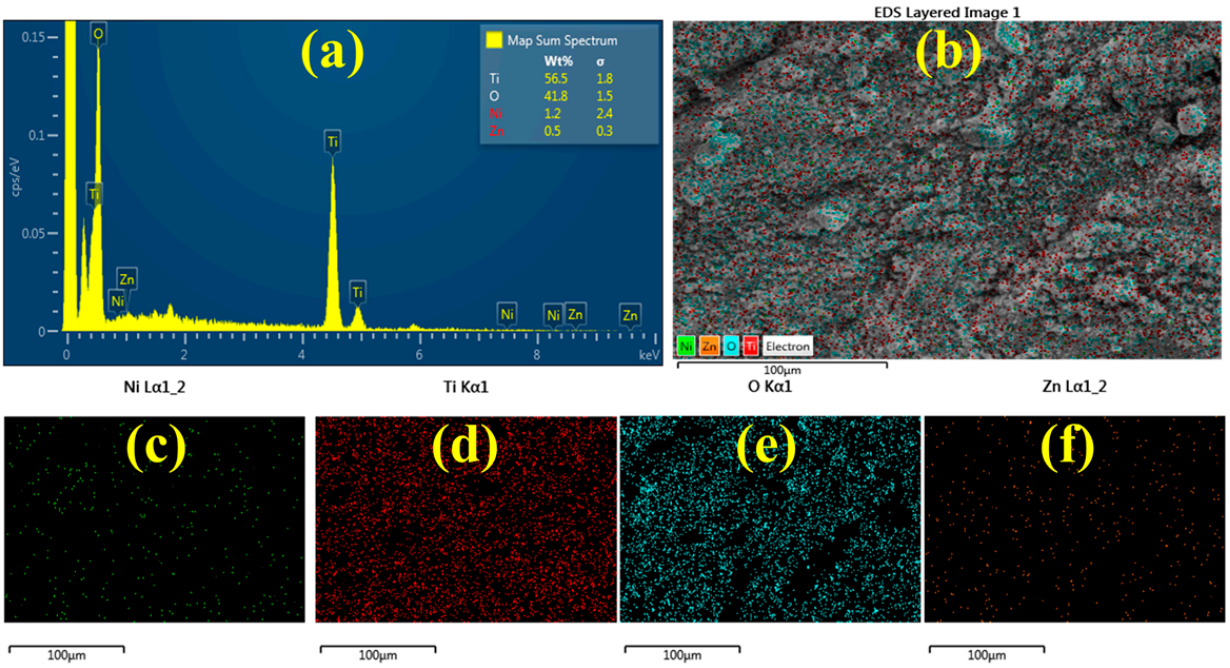


Figure 8. EDX spectrum (**a**) and colored elemental mapping (**b**–**f**) of the C-$NiTiO_2$ composite after Zn (II) ion adsorption.

2.4. Zn (II) Ion Selectivity and Reuse

For multi-element systems, where competition among different ions for adsorption sites occurs, selectivity towards specific metal ions can be evaluated. The adsorption equilibrium result for one type of metal ions existing with other metal ions is assessed by

the share of its adsorbed quantity in a mixture to that in a single-ion state. The influence of divalent Cu (II) and Cd (II) ions on Zn (II) ion uptake using C-$NiTiO_2$ composites was assessed using controlled laboratory samples in two- and three-ion type mixtures (Figure 9a). The selectivity for metal ion adsorption is verified by the ratio of the amount adsorbed in a mixture ($q_{e,m}$) to that in a single state (q_e). Based on the $q_{e,m}/q_e$ value, the impact of coexisting ions can be labeled as synergistic, antagonistic, or non-interactive when $q_{e,m}/q_e$ is >1, <1, or =1, respectively. The competitive adsorption fractions ($q_{e,m}/q_e$) for Zn (II) ions in the existence of rival ions are listed in Table 7. In the binary systems, $q_{e,m}/q_e < 1$ indicates an antagonistic impact of Cu (II) and Cd(II) ions on Zn (II) ion uptake. Nonetheless, the ratio was lower in the presence of Cd^{2+} ions, which indicates a greater impeding impact on Zn (II) removal. In the ternary combination, the ratio was lower compared to the binary combination, denoting more reduction in Zn (II) ion adsorption due to the ions of Cu (II) and Cd (II). The observed reduction in Zn (II) ion adsorption in ternary mixtures may be associated with the rise in repulsive interactions among ions, the screening effects of metal cations that suppress sorption, and competition with Cu (II) and Cd (II) ions for accessible adsorption sites. The selectivity of C-$NiTiO_2$ for Zn (II) ions over Cu^{2+} and Cd^{2+} ions can be accredited to some key physicochemical characteristics. Zn (II)has the lowest hydration energy (-2200 kJ·mol^{-1}) among the three metal ions, meaning it dehydrates more readily to interact with the adsorbent surface [57]. Moreover, Zn (II) has the smallest hydrated ionic radius (0.419 nm), which secures stronger electrostatic interactions and facile contact to adsorption sites within the adsorbent [58]. These factors jointly explicate the perceived adsorption selectivity for Zn (II) ions in a competitive setup.

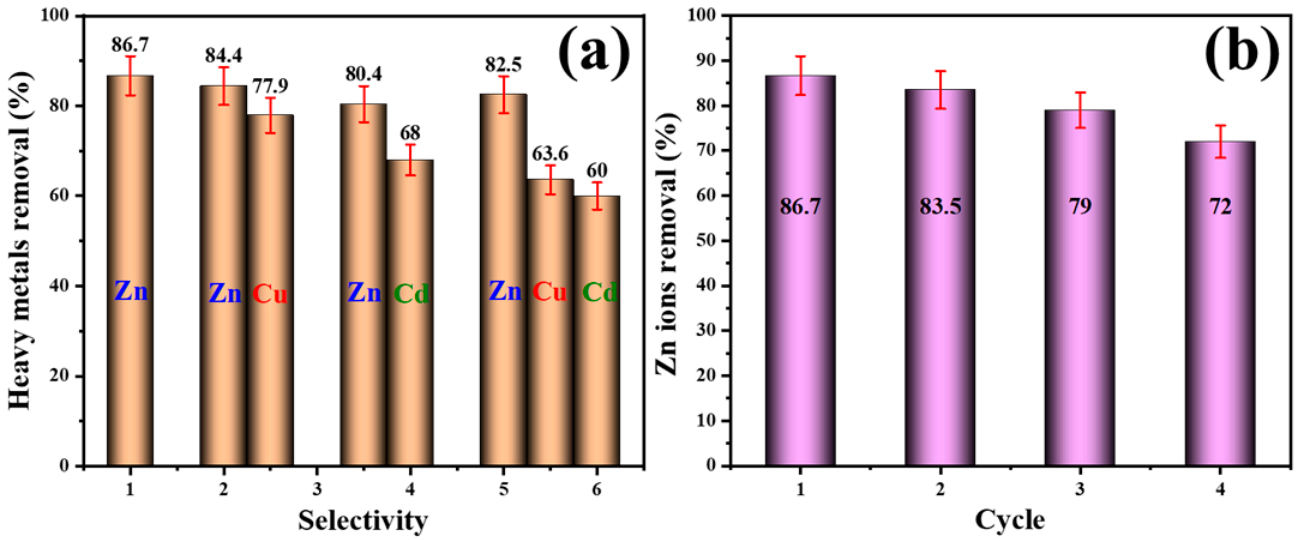


Figure 9. C-$NiTiO_2$ composite selectivity (**a**) and recyclability (**b**) for Zn (II) ion adsorption.

Table 7. Competitive adsorption values in single, binary, and ternary metal ion sets.

System Used	M^{n+}	Zn % Removal	$q_{e,m}/q_e$
Single	Zn	86.7	1.0
Binary	Zn–Cu	84.4	0.976
	Zn–Cd	80.4	0.929
Ternary	Zn–Cu–Cd	82.5	0.952

Besides the high adsorption efficiency of an adsorbent toward metal ions, regeneration and reusability are also outstanding and distinctive features of a good adsorbent. Adsorption–desorption activity is an important factor for assessing the proficiency, re-

juvenation capability, regeneration, reutilization, and economic benefits of invented adsorbents [59]. Adsorbents that are non-recyclable over multiple cycles or have declining adsorption capacity when reused may engender secondary environmental pollution and lead to high application costs. As shown in Figure 9b, the adsorption efficiency of C-$NiTiO_2$ marginally declined after each regeneration and reuse cycle. The use of 0.02 M HCl as a desorption agent is due to its ability to protonate the adsorbent's functional groups, thereby breaking coordination bonds with Zn (II) ions. The low concentration was chosen to accomplish efficient desorption while decreasing potential degradation of the adsorbent structure [60]. After four repeated adsorption–desorption cycles, the regenerated composite maintained ~72% of its original adsorption capacity, indicating excellent reusability with only a 14.7% decline in efficiency. The maintained adsorption efficiency (~72%) after four consecutive adsorption–desorption cycles validates the excellent recyclability, stability [61], and regeneration potential [62] of the C-$NiTiO_2$ composite, which is an important criterion for practical wastewater treatment applications. The reuse study was evaluated for each detection/sorption–elution–regeneration cycle, and the sorption efficacy in each cycle was assessed relative to the first sorption cycle. The recovery % values for the adsorbent were 96.3%, 94.6%, and 91%. Based on these obtained results for analogous sorption and elution processes, it can be concluded that C-$NiTiO_2$ can be used for many cycles as a cost-effective adsorbent in practical operations. Thus, the C-$NiTiO_2$ composite exhibits improved long-term stability and reusability as a prospective candidate for Zn (II) ion elimination from water samples [63,64].

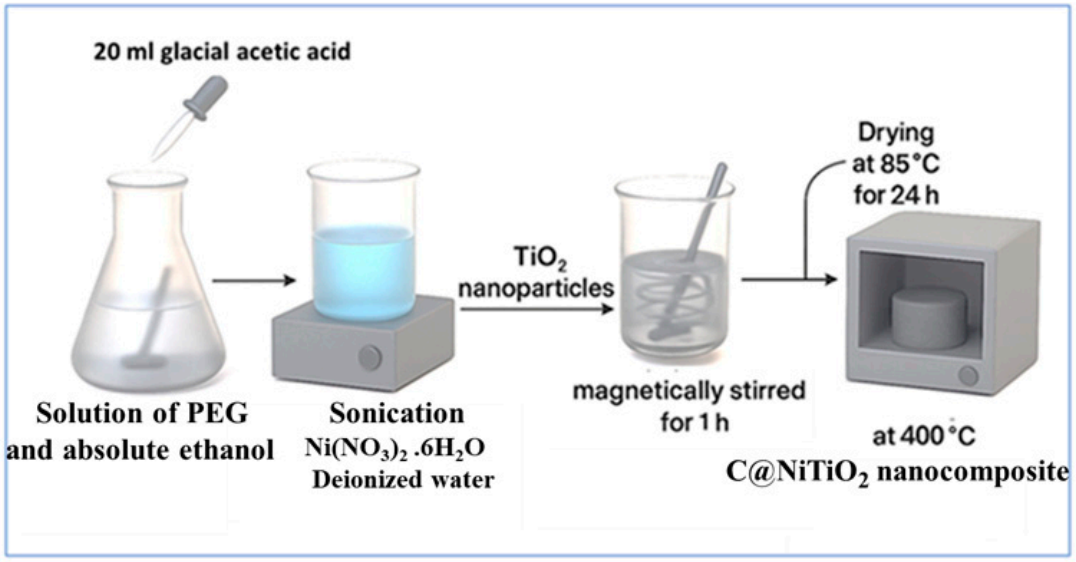
3. Materials and Methods

3.1. Materials

Zinc nitrate (Zn $(NO_3)_2$, 99%), nickel nitrate (Ni$(NO_3)_2$, 99%), acetic acid (CH_3COOH, 99%), polyethylene glycol ($HO(CH_2CH_2O)_nH$, 3600–4400), sodium hydroxide (NaOH), hydrochloric acid (HCl, 37%), and titanium dioxide (TiO_2) were acquired from Sigma-Aldrich. Absolute methanol (CH_3OH, 99%) was procured from Merck Chemical. All reagents were of analytical quality and utilized without additional purification. These materials were utilized in both the synthesis and adsorption studies.

3.2. C-$NiTiO_2$ Nanosorbent Fabrication

By means of a sol–gel-assisted technique, a nanocomposite composed of carbon, NiO, and TiO_2 nanoparticles was successfully manufactured. The first step in the synthesis process involved dissolving 8 g of polyethylene glycol (PEG) as a carbon source in 120 mL of 100% ethanol. After that, 20 mL of acetic acid was added while the mixture was continuously stirred until it reaches a fully homogeneous state. At the same time, a different solution was created by sonicating 1.25 g of nickel nitrate hexahydrate ($Ni(NO_3)_2 \cdot 6H_2O$) in 80 mL of distilled water for a duration of 20 min to guarantee completely dissolution. After that, 10.5 g of titanium dioxide nanoparticles was mixed into the solution while being stirred magnetically for 30 min to ensure uniform distribution. To create a well-mixed sol, the two solutions were first combined and then subjected to magnetic stirring for 60 min. The resulting mixture was heated at 85 °C for 24 h to facilitate gelation and structural consolidation. After filtering and drying the gel that was obtained, it was subjected to annealing at a temperature of 400 °C for 2 h in air (more details are shown in Scheme 2). This resulted in the final C-$NiTiO_2$ nanosorbent, which exhibited improved crystallinity and interfacial bonding. Calcination of carbon-doped nanoparticles at 400 °C gives nanostructures with optimal activity [65].



Scheme 2. Fabrication steps of C-$NiTiO_2$ nanosorbent.

3.3. Characterizations

The X-ray diffraction (XRD) technique utilized Bruker AXS equipment from Bruker (Karlsruhe, Germany) to analyze the crystal structure and phase purity of the C-$NiTiO_2$ nanosorbent by scanning diffraction angles from 10° to 80° at 2° per minute using Cu-Kα X-ray radiation, with a wavelength of 1.5418 Å, at an applied voltage of 40 kV and a current of 40 mA. The Brunauer–Emmett–Teller (BET) method was utilized to determine the surface area and porosity of the nanopowders using an ASAP 2020HD 88 apparatus (Micromeritics, Norcross, GA, USA). Before analysis, the powdered samples were subjected to a drying process under a continuous stream of N_2 at a temperature of 60 °C for 24 h. Energy-dispersive X-ray spectroscopy (EDX) was performed on a field emission scanning electron microscope (S-3400 N, Hitachi, Kawasaki, Japan), to conduct elemental chemical analysis of the nanocomposite. Transmission electron microscopy (TEM) analysis of the C-$NiTiO_2$ nanosorbent powder morphology was carried out using Tecnai G20 (FEI Tecnai, Hillsboro, OR, USA). A Nicolet 5700 Fourier transform infrared (FT-IR) spectrophotometer (Thermo Fisher Scientific, Waltham, MA, USA) was employed to examine the vibrational modes of the C-$NiTiO_2$ nanosorbent prior to and during the adsorption of Zn ions. Raman analysis was performed using a Renishaw inVia™ laser Raman instrument (Renishaw, Gloucestershire, UK) connected to a Leica DMLM microscope (Leica, Wetzlar, Germany). Rayleigh scattering was eliminated using an edge filter, and Raman scattering was dispersed by an 18,000 lines/mm holographic grating and detected by a charge-coupled device (CCD). A standard silicon wafer sample was used to calibrate the instrument by matching the 520.5 cm^{-1} band position, followed by manually aligning the laser beam with the crosshairs on the microscope. A 514.5 nm argon-ion green laser was used, delivering ~20 mW at 100% power. Hyperspectral infrared images were recorded using a Nicolet 5700 FTIR microscope system from Agilent Technologies (Mulgrave, Victoria, Australia) equipped with a 128 × 128 pixel FPA (mercury–cadmium–telluride) detector and a 32× Cassegrain objective. Spectra were recorded over the spectral range of 3800–950 cm^{-1} at a spectral resolution of 4 cm^{-1} for KBr pellets of C-$NiTiO_2$. Structural morphology and elemental distribution were analyzed using scanning electron microscopy and energy-dispersive spectroscopy (Tecnai G20). The prepared materials were air-dried and affixed on aluminum stubs using double-sided carbon adhesive tape. To mitigate charging effects and enhance conductivity, samples were sputter-coated with a thin gold layer of ≈5–10 nm under vacuum. SEM images were captured at 15–20 kV in high-vacuum mode, with magnifications

chosen to illustrate surface morphology. The point of zero charge (pHPZC) of C-$NiTiO_2$ nanostructures was ascertained utilizing the salt addition approach [66]. A succession of glass bottles was filled with a fixed volume of sodium chloride (NaCl) solution (10 mL, 0.2 mol·L^{-1}), and the initial pH was adjusted to 1, 2, 3, 4, 5, 6, 7, 8, 9, 10, 11, and 12 using either 0.1 mol L^{-1} NaOH or 0.1 mol L^{-1} HCl solution. Each bottle was thereafter filled with 10 mg of adsorbent and agitated continuously for 12 h at 25 °C. After filtration, the pH of each solution (pHf) was ascertained. The pH difference (ΔpH = pHf − pHi) was calculated and subsequently graphed against pHi, leading to the determination of the pHPZC value.

3.4. Zn (II) Ion Adsorption

Zn (II) ion adsorption details were achieved by decomposing specified quantities of Zn $(NO_3)_2$ in Milli-Q ultrapure water (with a resistivity of 18 MΩ·cm), resulting in stock solutions containing 1000 mg L^{-1} of Zn (II) ions. Serial dilutions of the stock solution yielded working solutions with initial Zn (II) ion concentrations between 5 and 200 mg L^{-1}. The pH of each solution was adjusted to the proper level using either 0.1 mol·L^{-1} sodium hydroxide or 0.1 mol·L^{-1} hydrochloric acid. All reagents employed were of analytical quality. To conduct equilibrium studies, several glass jars containing 50 mL were positioned on a magnetic stirrer. At a stirring velocity of 400 rpm per min, 25 mL of zinc ion solution with beginning concentrations of 5, 15, 30, 45, 60, 100, or 200 mg L^{-1} was amalgamated with 10 mg of C-$NiTiO_2$ adsorbent for each test. To ensure equilibrium, the contact time varied from 5 to 1440 min. Upon concluding the equilibration process, the suspensions underwent filtration via syringe filters with a pore size of 0.45 µm. Residual Zn (II) ion concentrations were concurrently evaluated using a Varian AAS240FS model Atomic Absorption Spectrometer (AAS) machine (Agilent Technologies, Santa Clara, CA, USA). Increasing the agitation speed increases the diffusion rate of adsorbate molecules from the bulk liquid to the liquid boundary layer surrounding the activated carbon particle due to the increased turbulence, thereby decreasing boundary layer thickness around the adsorbent particles as a result of an increased degree of mixing. However, increasing the agitation rate beyond a certain threshold leads to fragmentation of the adsorbent particles [67].

3.5. Statistical Analysis of Errors

All the experiments were performed in triplicate sets, and the standard deviation (σ) was calculated as follows:

$$\sigma = \sqrt{\sum_{i=1}^{n} \frac{(x_i - \mu)^2}{N}} \quad (9)$$

The symbols *xi*, *u*, and *N* denote individual value, mean value, and number of points in the population, respectively. Nonlinear regression analysis of the kinetic and isotherm model data was performed to validate the agreement between theoretical adsorption models and experimental adsorption data. The nonlinear regression analysis was fitted by using the Solver add-in function of Microsoft Excel software. Statistical error functions, such as the coefficient of determination (R^2) and the residual sum of squares (RSSs), were used to evaluate the fitting of adsorption model formulae from experimental data in assessing the model variables. The R^2 and RSS are given as follows:

$$R^2 = \frac{\sum_{i=1}^{N} \left(q_{exp,i} - q_{cal,i}\right)^2}{\sum_{i=1}^{N} \left(q_{e,exp}\right)^2 - \left[\left(\sum_{i=1}^{N} q_{exp,i}\right)^2\right]/N} \quad (10)$$

$$RSS = \sum (\mathrm{yi} - \hat{\mathrm{y}}\mathrm{i})^2 \quad (11)$$

The symbols, 'exp', and 'cal' denote the mean, experimental, and theoretical qe quantities, respectively; yi is the observed value, ŷi is the predicted value, and n is the number of

observations in the experiment. An R^2 value of ≈1.0 and lower RSS values indicate a better fit of the model to the data. All experiments were performed in triplicate, and the average values were taken.

4. Conclusions

This study sought to produce a C-$NiTiO_2$ composite to eliminate Zn (II) ions in aqueous media. XRD analysis confirmed anatase as the major phase, while TEM detected carbon on the C-$NiTiO_2$ surface, manifested by the appearance of uniformly distributed tiny dots. N_2 adsorption technique verified the construction of a nanostructure with a mesoporous surface area of ≈17 $m^2 \cdot g^{-1}$, a pore diameter of ≈1.5 nm, and a pore volume of 0.0315 $cm^3 \cdot g^{-1}$. These structural characteristics enabled it to effectively adsorb zinc metal ions at pH = 3.5 using a 10 mg C-$NiTiO_2$ dose. Furthermore, the adsorption process could be described by two steps, and the two linear stages relevant to the interpolation of the experimental data did not directly cross the origin, validating favored adsorption on the outer surface of the composite. Equilibrium analyses confirmed that the adsorption model was in consonance with the Langmuir adsorption model, with an upmost loading of 369 $mg \cdot g^{-1}$, where the quasi-second-order kinetic model complied with the experimental data. The Boyd kinetic model verified that film diffusion was the dominant rate-controlling stepthe Zn (II) ions diffusion into the C-$NiTiO_2$ adsorbent, and that surface complexation, ion exchange, and electrostatic attraction were the postulated modes of interaction between Zn (II) ions with the C-$NiTiO_2$ composite. These aspects sanction the potential of the eco-friendly C-$NiTiO_2$ hybrid for operative metal ion eradication from aqueous solutions.

Author Contributions: Conceptualization, A.A.A. and A.M.; methodology, A.M.; software, A.A. (Abuzar Albadri); validation, A.S.A. and M.A.; formal analysis, T.M.A. and A.A. (Ajayb Alresheedi); investigation, A.A.A. and A.M.; resources, A.A.A.; data curation, T.M.A. and A.A. (Ajayb Alresheedi); writing—original draft preparation, A.M.; writing—review and editing, all authors; supervision, A.M.; project administration, A.A.A.; funding acquisition, A.A.A. All authors have read and agreed to the published version of the manuscript.

Funding: This research received no external funding.

Institutional Review Board Statement: Not applicable.

Informed Consent Statement: Not applicable.

Data Availability Statement: The data supporting the findings of this study are available within the article. Any additional information can be obtained from the corresponding author upon reasonable request.

Acknowledgments: All researchers would like to thank the Deanship of Graduate Studies and Scientific Research at Qassim University for financial support (QU-APC-2026).

Conflicts of Interest: The authors declare no conflicts of interest.

References

1. Kaur, J.; Sengupta, P.; Mukhopadhyay, S. Critical review of bioadsorption on modified cellulose and removal of divalent heavy metals (Cd, Pb, and Cu). *Ind. Eng. Chem. Res.* **2022**, *61*, 1921–1954. [CrossRef]
2. Ahuja, R.; Kalia, A.; Sikka, R.; P, C. Nano modifications of biochar to enhance heavy metal adsorption from wastewaters: A review. *ACS Omega* **2022**, *7*, 45825–45836. [CrossRef] [PubMed]
3. Efome, J.E.; Rana, D.; Matsuura, T.; Lan, C.Q. Insight studies on metal-organic framework nanofibrous membrane adsorption and activation for heavy metal ions removal from aqueous solution. *ACS Appl. Mater. Interfaces* **2018**, *10*, 18619–18629. [CrossRef] [PubMed]
4. Çelebi, H.; Gök, G.; Gök, O. Adsorption capability of brewed tea waste in waters containing toxic lead (II), cadmium (II), nickel (II), and zinc (II) heavy metal ions. *Sci. Rep.* **2020**, *10*, 17570. [CrossRef]

5. Akram, M.; Bano, Z.; Bhutto, S.U.A.; Pan, J.; Uddin, A.; Afzal, M.Z.; Li, L.; Xia, M.; Wang, F. Highly efficient nickel recovery from industrial wastewater via synergistic electrodeposition and electrocatalytic oxidation technique. *J. Environ. Chem. Eng.* **2024**, *12*, 112830. [CrossRef]
6. Hassan, M.; Liu, Y.; Naidu, R.; Du, J.; Qi, F.; Donne, S.W.; Islam, M.M. Mesoporous biopolymer architecture enhanced the adsorption and selectivity of aqueous heavy-metal ions. *ACS Omega* **2021**, *6*, 15316–15331. [CrossRef] [PubMed]
7. Zou, Y.; Wang, X.; Khan, A.; Wang, P.; Liu, Y.; Alsaedi, A.; Hayat, T.; Wang, X. Environmental remediation and application of nanoscale zero-valent iron and its composites for the removal of heavy metal ions: A review. *Environ. Sci. Technol.* **2016**, *50*, 7290–7304. [CrossRef]
8. Bano, Z.; Akram, M.; Ali, N.Z.; Khan, M.U.; Wang, F.; Li, L.; Xia, M. Sustainable porous graphene/Co-MOF for the removal of water pollutants: Combined theoretical and experimental studies. *J. Water Process Eng.* **2024**, *59*, 104982. [CrossRef]
9. Crini, G.; Lichtfouse, E. Advantages and disadvantages of techniques used for wastewater treatment. *Environ. Chem. Lett.* **2019**, *17*, 145–155. [CrossRef]
10. Hawrysz, Z.; Woźniacka, A. Zinc: An undervalued microelement in research and treatment. *Adv. Dermatol. Allergol./Postępy Dermatol. I Alergol.* **2023**, *40*, 208–214. [CrossRef]
11. Vasylyeva, H.; Mironyuk, I.; Mykytyn, I.; Danyliyk, N. Adsorption of barium and zinc ions by mesoporous TiO_2 with chemosorbed carbonate groups. *Phys. Chem. Solid State* **2019**, *20*, 282–290. [CrossRef]
12. Bożena, G.; Zakrzewska, D.; Szymczycha, B. Sorption of Cr, Pb, Cu, Zn, Cd, Ni, and Co to nano-TiO_2 in seawater. *Water Sci. Technol.* **2018**, *77*, 145–158. [CrossRef] [PubMed]
13. Chen, J.; Zhang, L.; Zhu, J.; Wang, N.; Feng, J.; Yan, W. Adsorption of polythiophene/TiO_2 composite for Zn (II), Pb (II) and Cu (II): Selectivity and synergistic effect investigation. *Appl. Surf. Sci.* **2018**, *459*, 318–326. [CrossRef]
14. Kumordzi, G.; Malekshoar, G.; Yanful, E.K.; Ray, A.K. Solar photocatalytic degradation of Zn^{2+} using graphene based TiO_2. *Sep. Purif. Technol.* **2016**, *168*, 294–301. [CrossRef]
15. Rana, P.; Jeevanandam, P. Synthesis of NiO nanoparticles via calcination of surfactant intercalated layered nickel hydroxides and their application as adsorbent. *J. Clust. Sci.* **2023**, *34*, 517–533. [CrossRef]
16. Abuhatab, S.; El-Qanni, A.; Al-Qalaq, H.; Hmoudah, M.; Al-Zerei, W. Effective adsorptive removal of Zn^{2+}, Cu^{2+}, and Cr^{3+} heavy metals from aqueous solutions using silica-based embedded with NiO and MgO nanoparticles. *J. Environ. Manag.* **2020**, *268*, 110713. [CrossRef]
17. Abdolmohammad-Zadeh, H.; Ayazi, Z.; Naghdi, Z. Nickel oxide/chitosan nano-composite as a magnetic adsorbent for pre-concentration of Zn (II) ions. *J. Magn. Magn. Mater.* **2019**, *488*, 165311. [CrossRef]
18. Zahan, N.; Fahim, S.A.; Shuvo, M.S.H.; Sarker, M.; Masum, S.M.; Molla, M.A.I. Fabrication and characterization of C–doped TiO_2 nanoparticles for the photodegradation of organic dyes. *Inorg. Nano-Met. Chem.* **2024**, *55*, 851–863. [CrossRef]
19. Lim, C.; An, H.-R.; Lee, H.; Lee, R.; Choi, Y.; Park, J.-I.; Yoon, J.; Lee, H.U.; Lee, Y.-S. Carbon-titanium dioxide heterogeneous (photo) catalysts (C–TiO_2) for highly efficient visible light photocatalytic application. *Compos. Part B Eng.* **2022**, *241*, 109997. [CrossRef]
20. Shaban, Y.A.; El Maradny, A.A.; Al Farawati, R.K. Photocatalytic reduction of nitrate in seawater using C/TiO_2 nanoparticles. *J. Photochem. Photobiol. A Chem.* **2016**, *328*, 114–121. [CrossRef]
21. Hassan, M.E.; Liu, G.; Omer, E.O.M.; Goja, A.M.; Acharya, S. Silver embedded C-TiO_2 exhibits improved photocatalytic properties with potential application in waste water treatment. *Arab. J. Chem.* **2019**, *12*, 1134–1140. [CrossRef]
22. Zhang, J.; Cui, F.; Xu, L.; Ma, Q.; Gao, Y.; Liu, Y.; Cui, T. Construction of magnetic NiO/C nanosheets derived from coordination polymers for extraordinary adsorption of dyes. *J. Colloid Interface Sci.* **2020**, *561*, 542–550. [CrossRef] [PubMed]
23. Lu, H.; Zhang, L.; Ma, J.; Alam, N.; Zhou, X.; Ni, Y. Nano-cellulose/MOF derived carbon doped CuO/Fe_3O_4 nanocomposite as high efficient catalyst for organic pollutant remedy. *Nanomaterials* **2019**, *9*, 277. [CrossRef]
24. Ellouzi, I.; El Hajjaji, S.; Harir, M.; Schmitt Koplin, P.; Robert, D.; Laânab, L. Synergistic effects of C, N, S, Fe-multidoped TiO_2 for photocatalytic degradation of methyl orange dye under UV and visible light irradiations. *SN Appl. Sci.* **2019**, *1*, 930. [CrossRef]
25. Tan, Y.; Xu, H.; Shu, R.; Liu, Z.; Song, L.; Zhang, R.; Ouyang, C.; Xia, M.; Hou, J.; Zhang, X. Synergistic effects of multitype carbon doping and oxygen vacancies in TiO_2/CNTs composite fabricated via nonthermal plasma for formaldehyde removal. *Chemosphere* **2023**, *337*, 139406. [CrossRef] [PubMed]
26. Oginawati, K.; Susetyo, S.H.; Sulung, G.; Chazanah, N.; Kusumah, S.W.D.; Fahimah, N. Investigation of dermal exposure to heavy metals (Cu, Zn, Ni, Al, Fe and Pb) in traditional batik industry workers. *Heliyon* **2022**, *8*, e08914. [CrossRef]
27. Schoofs, H.; Schmit, J.; Rink, L. Zinc toxicity: Understanding the limits. *Molecules* **2024**, *29*, 3130. [CrossRef]
28. Vasylyeva, H.; Mironyuk, I.; Mykytyn, I.; Danylyuk, N. Адсорбція йонів барію та цинку мезопористим TiO_2 з хемосорбованими карбонатними групами. *фізика* і хімія твердого тіла **2019**, *20*, 282–290. [CrossRef]
29. Mironyuk, I.; Mykytyn, I.; Vasylyeva, H.; Savka, K. Sodium-modified mesoporous TiO_2: Sol-gel synthesis, characterization and adsorption activity toward heavy metal cations. *J. Mol. Liq.* **2020**, *316*, 113840. [CrossRef]

30. Charpentier, T.V.; Neville, A.; Lanigan, J.L.; Barker, R.; Smith, M.J.; Richardson, T. Preparation of magnetic carboxymethylchitosan nanoparticles for adsorption of heavy metal ions. *ACS Omega* **2016**, *1*, 77–83. [CrossRef]
31. Thakur, N.; Arya, V.; Kumar, A.; Thakur, N. Catalytic efficiency of encapsulated coupled doped Zn-Ni TiO_2 nanocatalyst for the removal of organic pollutants and free radical assay. *Int. J. Environ. Anal. Chem.* **2024**, *104*, 9754–9771. [CrossRef]
32. Ragesh Nath, R.; Nethravathi, C.; Rajamathi, M. Hierarchically porous, biphasic, and C-Doped TiO_2 for solar photocatalytic degradation of dyes and selective oxidation of benzyl alcohol. *ACS Omega* **2021**, *6*, 12124–12132. [CrossRef]
33. Sheshmani, S.; Nayebi, M. Modification of TiO_2 with graphene oxide and reduced graphene oxide; enhancing photocatalytic activity of TiO_2 for removal of remazol Black B. *Polym. Compos.* **2019**, *40*, 210–216. [CrossRef]
34. Alkorbi, A.S.; Javed, H.M.A.; Hussain, S.; Latif, S.; Mahr, M.S.; Mustafa, M.S.; Alsaiari, R.; Alhemiary, N.A. Solar light-driven photocatalytic degradation of methyl blue by carbon-doped TiO_2 nanoparticles. *Opt. Mater.* **2022**, *127*, 112259. [CrossRef]
35. Dasgupta, N.P.; Neubert, S.; Lee, W.; Trejo, O.; Lee, J.-R.; Prinz, F.B. Atomic layer deposition of Al-doped ZnO films: Effect of grain orientation on conductivity. *Chem. Mater.* **2010**, *22*, 4769–4775. [CrossRef]
36. Trenczek-Zajac, A.; Synowiec, M.; Zakrzewska, K.; Zazakowny, K.; Kowalski, K.; Dziedzic, A.; Radecka, M. Scavenger-supported photocatalytic evidence of an extended type I electronic structure of the TiO_2@Fe_2O_3 interface. *ACS Appl. Mater. Interfaces* **2022**, *14*, 38255–38269. [CrossRef] [PubMed]
37. El Bendali, A.; Aqil, M.; Hdidou, L.; El Halya, N.; El Ouardi, K.; Alami, J.; Boschetto, D.; Dahbi, M. The electrochemical and structural changes of phosphorus-doped TiO_2 through in situ Raman and in situ X-ray diffraction analysis. *ACS Omega* **2024**, *9*, 14911–14922. [CrossRef]
38. Peng, X.-W.; Zhong, L.-X.; Ren, J.-L.; Sun, R.-C. Highly effective adsorption of heavy metal ions from aqueous solutions by macroporous xylan-rich hemicelluloses-based hydrogel. *J. Agric. Food Chem.* **2012**, *60*, 3909–3916. [CrossRef]
39. Li, X.; Li, H.; Yang, G. Configuration, anion-specific effects, diffusion, and impact on counterions for adsorption of salt anions at the interfaces of clay minerals. *J. Phys. Chem. C* **2016**, *120*, 14621–14630. [CrossRef]
40. He, G.; Pan, G.; Zhang, M.; Waychunas, G.A. Coordination Structure of Adsorbed Zn (II) at Water–TiO_2 interfaces. *Environ. Sci. Technol.* **2011**, *45*, 1873–1879. [CrossRef]
41. Nie, Z.; Finck, N.; Heberling, F.; Pruessmann, T.; Liu, C.; Lützenkirchen, J. Adsorption of selenium and strontium on goethite: EXAFS study and surface complexation modeling of the ternary systems. *Environ. Sci. Technol.* **2017**, *51*, 3751–3758. [CrossRef]
42. Jiang, C.; Wang, X.; Hou, B.; Hao, C.; Li, X.; Wu, J. Construction of a lignosulfonate–lysine hydrogel for the adsorption of heavy metal ions. *J. Agric. Food Chem.* **2020**, *68*, 3050–3060. [CrossRef] [PubMed]
43. Abdel Salam, M.; Abukhadra, M.R.; Adlii, A. Insight into the adsorption and photocatalytic behaviors of an organo-bentonite/Co_3O_4 green nanocomposite for malachite green synthetic dye and Cr (VI) metal ions: Application and mechanisms. *ACS Omega* **2020**, *5*, 2766–2778. [CrossRef] [PubMed]
44. Yuan, T.; Wei, W.; Jiang, W.; Wang, W. Vertical diffusion of ions within single particles during electrochemical charging. *ACS Nano* **2021**, *15*, 3522–3528. [CrossRef] [PubMed]
45. Town, R.M.; Van Leeuwen, H.P.; Duval, J.F. Rigorous physicochemical framework for metal ion binding by aqueous nanoparticulate humic substances: Implications for speciation modeling by the NICA-donnan and WHAM codes. *Environ. Sci. Technol.* **2019**, *53*, 8516–8532. [CrossRef]
46. Chu, K.H.; Hashim, M.A.; Hayder, G. Boyd's film diffusion model for water contaminant adsorption: Time for an upgrade? *J. Mol. Liq.* **2024**, *409*, 125466. [CrossRef]
47. Raji, Z.; Karim, A.; Karam, A.; Khalloufi, S. Adsorption of heavy metals: Mechanisms, kinetics, and applications of various adsorbents in wastewater remediation—A review. *Waste* **2023**, *1*, 775–805. [CrossRef]
48. Elias Carvalho, M.M.C.; Soares, L.C.; Adarme, O.F.H.; Ferreira, G.M.D.; Savedra, R.M.L.; Siqueira, M.F.; Azevedo, E.R.d.; Gurgel, L.V.A. Hetero-Disubstituted Sugarcane Bagasse as an Efficient Bioadsorbent for Cationic Dyes. *Molecules* **2025**, *30*, 3163. [CrossRef]
49. Bashir, A.; Manzoor, T.; Malik, L.A.; Qureashi, A.; Pandith, A.H. Enhanced and selective adsorption of Zn (II), Pb (II), Cd (II), and Hg (II) ions by a dumbbell-and flower-shaped potato starch phosphate polymer: A combined experimental and DFT calculation study. *ACS Omega* **2020**, *5*, 4853–4867. [CrossRef]
50. Cholico-Gonzalez, D.; Ortiz Lara, N.; Fernandez Macedo, A.M.; Chavez Salas, J. Adsorption behavior of Pb (II), Cd (II), and Zn (II) onto agave bagasse, characterization, and mechanism. *ACS Omega* **2020**, *5*, 3302–3314. [CrossRef]
51. Melo, D.Q.; Neto, V.O.; Oliveira, J.T.; Barros, A.L.; Gomes, E.C.; Raulino, G.S.; Longuinotti, E.; Nascimento, R.F. Adsorption equilibria of Cu2+, Zn2+, and Cd2+ on EDTA-functionalized silica spheres. *J. Chem. Eng. Data* **2013**, *58*, 798–806. [CrossRef]
52. Putra, W.P.; Kamari, A.; Yusoff, S.N.M.; Ishak, C.F.; Mohamed, A.; Hashim, N.; Isa, I.M. Biosorption of Cu (II), Pb (II) and Zn (II) ions from aqueous solutions using selected waste materials: Adsorption and characterisation studies. *J. Encapsulation Adsorpt. Sci.* **2014**, *4*, 25–35. [CrossRef]
53. Chen, H.; Zhao, Y.; Yang, Q.; Yan, Q. Preparation of poly-ammonium/sodium dithiocarbamate for the efficient removal of chelated heavy metal ions from aqueous environments. *J. Environ. Chem. Eng.* **2018**, *6*, 2344–2354. [CrossRef]

54. Anitha, T.; Senthil Kumar, P.; Sathish Kumar, K. Binding of Zn (II) ions to chitosan–PVA blend in aqueous environment: Adsorption kinetics and equilibrium studies. *Environ. Prog. Sustain. Energy* **2015**, *34*, 15–22. [CrossRef]
55. Zhu, H.; Chen, S.; Luo, Y. Adsorption mechanisms of hydrogels for heavy metal and organic dyes removal: A short review. *J. Agric. Food Res.* **2023**, *12*, 100552. [CrossRef]
56. Ciszak, C.; Mermoux, M.; Gutierrez, G.; Leprêtre, F.; Duriez, C.; Popa, I.; Fayette, L.; Chevalier, S. Raman spectra analysis of ZrO_2 thermally grown on Zircaloy substrates irradiated with heavy ion: Effects of oxygen isotopic substitution. *J. Raman Spectrosc.* **2019**, *50*, 425–435. [CrossRef]
57. Marcus, Y. Thermodynamics of solvation of ions. Part 5.—Gibbs free energy of hydration at 298.15 K. *J. Chem. Soc. Faraday Trans.* **1991**, *87*, 2995–2999. [CrossRef]
58. Awual, M.R.; Hasan, M.M.; Islam, A.; Rahman, M.M.; Asiri, A.M.; Khaleque, M.A.; Sheikh, M.C. Offering an innovative composited material for effective lead (II) monitoring and removal from polluted water. *J. Clean. Prod.* **2019**, *231*, 214–223. [CrossRef]
59. Awual, M.R. A facile composite material for enhanced cadmium (II) ion capturing from wastewater. *J. Environ. Chem. Eng.* **2019**, *7*, 103378. [CrossRef]
60. González, J.A.; Villanueva, M.E.; Piehl, L.L.; Copello, G.J. Development of a chitin/graphene oxide hybrid composite for the removal of pollutant dyes: Adsorption and desorption study. *Chem. Eng. J.* **2015**, *280*, 41–48. [CrossRef]
61. Islam, A.; Shahriar, M.; Islam, M.T.; Islam, T.; Papia, A.; Mohanta, S.C.; Khan, M.A.R.; Rahman, M.A.; Kubra, K.T.; Hasan, M.M. Recent breakthroughs and future horizons in next-generation HT-PEMs for hydrogen fuel cell. *Int. J. Hydrogen Energy* **2025**, *168*, 151113. [CrossRef]
62. Awual, M.R. Novel ligand functionalized composite material for efficient copper (II) capturing from wastewater sample. *Compos. Part B Eng.* **2019**, *172*, 387–396. [CrossRef]
63. Awual, M.R.; Hasan, M.M.; Znad, H. Organic–inorganic based nano-conjugate adsorbent for selective palladium (II) detection, separation and recovery. *Chem. Eng. J.* **2015**, *259*, 611–619. [CrossRef]
64. Awual, M.R.; Hasan, M.M.; Shahat, A.; Naushad, M.; Shiwaku, H.; Yaita, T. Investigation of ligand immobilized nano-composite adsorbent for efficient cerium (III) detection and recovery. *Chem. Eng. J.* **2015**, *265*, 210–218. [CrossRef]
65. Lin, Y.-T.; Weng, C.-H.; Lin, Y.-H.; Shiesh, C.-C.; Chen, F.-Y. Effect of C content and calcination temperature on the photocatalytic activity of C-doped TiO_2 catalyst. *Sep. Purif. Technol.* **2013**, *116*, 114–123. [CrossRef]
66. Bakatula, E.N.; Richard, D.; Neculita, C.M.; Zagury, G.J. Determination of point of zero charge of natural organic materials. *Environ. Sci. Pollut. Res.* **2018**, *25*, 7823–7833. [CrossRef]
67. Kuśmierek, K.; Świątkowski, A. The influence of different agitation techniques on the adsorption kinetics of 4-chlorophenol on granular activated carbon. *React. Kinet. Mech. Catal.* **2015**, *116*, 261–271. [CrossRef]

Disclaimer/Publisher's Note: The statements, opinions and data contained in all publications are solely those of the individual author(s) and contributor(s) and not of MDPI and/or the editor(s). MDPI and/or the editor(s) disclaim responsibility for any injury to people or property resulting from any ideas, methods, instructions or products referred to in the content.